

Squeezing water from a stone: H₂O in nominally anhydrous minerals from granulite xenoliths and deep, hydrous fractional crystallization

Emily Joyce Chin¹, Sean Taylor Curran¹, and G. Lang Farmer²

¹Scripps Institution of Oceanography

²University of Colorado Boulder

November 26, 2022

Abstract

Although ~10% of Earth's water resides within continents, HO distribution throughout the continental lithosphere and partitioning of HO in nominally anhydrous minerals (NAMs) remain poorly constrained. Models of continent formation and destruction depend on HO content. We report HO contents in NAMs measured on petrographic thin sections by secondary ion mass spectrometry (SIMS) of Proterozoic deep crustal xenoliths from Colorado, USA. Clinopyroxene, orthopyroxene, and garnet contain average HO contents of 560, 347, and 85 ppm, respectively; reconstructed bulk rock HO ranges from ~75 to ~600 ppm. Inter-mineral HO ratios overlap experimental mineral/melt D values, and are used to calculate HO of melts last in equilibrium with the xenoliths. We propose that these xenoliths represent cumulates fractionated from a primitive, hydrous ([?]₁ wt.% HO) melt at high (~1 GPa) pressures, similar to conditions in modern subduction zones, and potentially associated with widespread arc accretion that formed the core of North America in the Precambrian.

Hosted file

chincurranfarmer_si.docx available at <https://authorea.com/users/529841/articles/605506-squeezing-water-from-a-stone-h2o-in-nominally-anhydrous-minerals-from-granulite-xenoliths-and-deep-hydrous-fractional-crystallization>

1 **Squeezing water from a stone: H₂O in nominally anhydrous minerals**
2 **from granulite xenoliths and deep, hydrous fractional crystallization**

3 **Emily J. Chin¹, Sean T. Curran¹, and G. Lang Farmer³**

4 ¹Geosciences Research Division, Scripps Institution of Oceanography, University of
5 California, San Diego, La Jolla, CA, USA

6 ²Department of Geological Sciences and CIRES, University of Colorado Boulder, CO,
7 USA

8 Corresponding author: Emily J. Chin (e8schin@ucsd.edu)

9 **Key Points:**

- 10 • H₂O contents in cpx, opx, garnet in Proterozoic lower crustal xenoliths from
11 Colorado
- 12 • Mineral H₂O content used to reconstruct bulk rock and calculate melt H₂O
- 13 • Xenoliths represent metamorphosed igneous cumulates from high-P, hydrous
14 magmas
15

16 Abstract

17 Although ~10% of Earth's water resides within continents, H₂O distribution throughout
18 the continental lithosphere and partitioning of H₂O in nominally anhydrous minerals
19 (NAMs) remain poorly constrained. Models of continent formation and destruction
20 depend on H₂O content. We report H₂O contents in NAMs measured *in situ* on
21 petrographic thin sections by secondary ion mass spectrometry (SIMS) of Proterozoic
22 deep crustal xenoliths from Colorado, USA. Clinopyroxene, orthopyroxene, and garnet
23 contain average H₂O contents of 560, 347, and 85 ppm, respectively; reconstructed bulk
24 rock H₂O ranges from ~75 to ~600 ppm. Inter-mineral H₂O ratios overlap experimental
25 mineral/melt D values, and are used to calculate H₂O of melts last in equilibrium with the
26 xenoliths. We propose that these xenoliths represent cumulates fractionated from a
27 primitive, hydrous (≥ 1 wt.% H₂O) melt at high (~1 GPa) pressures, similar to conditions
28 in modern subduction zones, and potentially associated with widespread arc accretion
29 that formed the core of North America in the Precambrian.

30

31 1 Introduction

32 Water is key to plate tectonics on Earth, which, in turn, is vital to the production of
33 continental crust. Yet debate continues over when plate tectonics and arc-related
34 continental crust formation began, with estimates ranging widely from as late as 800 Ma
35 to as early as ~4 Ga (Arndt, 2013). Processes such as intraplate/plume magmatism and
36 accretion of oceanic plateaus have thus been proposed in contrast to the arc model of
37 continental growth (Rudnick, 1995). An important aspect of this debate involves the
38 formation and evolution of lower continental crust – particularly, the nature of magmas
39 that first encounter the Moho prior to further differentiation, and the solids such magmas
40 leave behind. The budget and trajectory of magmatic water in the deep crust has
41 profound consequences for cumulate mineralogy, lower crustal rheology, and ultimately
42 bulk crustal composition. For instance, higher magmatic water expands the liquidus field
43 of pyroxene over plagioclase (Kushiro & Yoder, 1969), resulting in pyroxenite cumulates
44 dominating arc lower crust, compared to plagioclase-rich cumulates in oceanic lower
45 crust (Chin et al., 2018). Water also plays an important role in crusting melting (Collins
46 et al., 2020). Lastly, even at ppm levels, water in mineral lattices can significantly
47 enhance crystal plasticity and decrease rock viscosity (Hirth & Kohlstedt, 1995), thereby
48 promoting deformation, and may thus contribute to de-stabilization of dense, mafic crust
49 and the survival of buoyant, felsic continental crust.

50 Knowledge of the initial water content of primary magmas should allow us to discern
51 whether continental crust formed via a hydrous process (subduction) versus anhydrous
52 processes (plumes, ridges), because water content of primary magmas is an important
53 discriminator for subduction vs. non-subduction settings (Sobolev & Chaussidon, 1996).
54 The problem is that determining the water content of a primary magma is challenging,
55 because such magmas are rarely, if ever, directly sampled. An alternative perspective is
56 provided by deep crustal xenoliths that represent early fractionated magmatic cumulates
57 or restites. Because they are denser than melts, cumulates are left behind in the deep
58 crust, preserving a record of early magmatic processes. Such a record is obscured in
59 shallowly emplaced magmas that traverse, and potentially assimilate, thick and
60 heterogeneous crust. Primitive crystalline solids (cumulates) fractionated from magmas
61 offer a glimpse into the trace element and volatile content of melts these cumulates were
62 last in equilibrium with (Chin et al., 2018), if the partitioning of trace elements and
63 volatiles between cumulate minerals and melt is known, and if such cumulates were not
64 later re-hydrated or metasomatized.

65 We propose the following testable hypotheses wherein deep crustal cumulates could
66 be used to distinguish initially hydrous melts versus anhydrous melts, thus using such
67 cumulates to discriminate tectonic setting. In a subduction zone, primary magmas start
68 wet – already containing at least ~2 wt. % H₂O (Plank et al., 2013). Subsequent
69 fractional crystallization evolves more hydrous derivative melts that have been shown to
70 fractionate garnet and clinopyroxene-rich cumulates in the lower crust (Lee et al., 2006;
71 Muntener & Ulmer, 2006) and amphibole-rich cumulates in the middle crust (Davidson
72 et al., 2007). Igneous cumulates and restites are increasingly recognized as an important
73 driver for refining continental crust to silica-rich compositions, particularly if such
74 cumulates contain large amounts of garnet to render them convectively unstable (Lee &
75 Anderson, 2015), allowing them to founder, leaving behind less dense, Si-rich crust.
76 Relics of lower crustal foundering may exist in cumulates that deformed by high-
77 temperature plastic deformation, or may have been deformed when the lithosphere
78 thickened to pressures high enough to stabilize garnet (Chin et al., 2016). By contrast, in
79 a non-subduction setting such as a plume, primary melts would be predicted to be drier
80 compared to melts generated in subduction zones, due to larger extent of melting, which

81 would dilute the initial H₂O content of mantle-derived melts. Water contents of primary
82 intraplate magmas are highly variable, spanning the entire range from MORB-like to arc-
83 like (Liu et al., 2017); this may stem from heterogeneity of deep mantle reservoirs.
84 Cumulates that fractionate from flood basalts appear to fall along tholeiitic trends
85 dominated by olivine fractionation (Rehfeldt et al., 2007). In addition, igneous cumulates
86 might exhibit limited evidence of plastic deformation if they formed in a plume setting
87 (Tommasi & Ishikawa, 2014).

88 Here, we address the interrelated issues of the hydration state of the lower continental
89 crust and continental crust formation processes by examining a suite of granulite
90 xenoliths from the Devonian-age State Line Kimberlite District, northern Colorado, USA.
91 Our samples are ideal for constraining the water content of stable continental lower crust
92 because they record Proterozoic crustal formation ages, and, importantly, erupted well
93 before the Cenozoic Laramide Orogeny, which is thought to have caused a widespread
94 hydrous overprint of the deep lithosphere beneath Western North America (Jones et al.,
95 2015; Li et al., 2008). An evaluation of previously published bulk rock major element
96 data, combined with new clinopyroxene major element data and H₂O contents in NAMs
97 analyzed by secondary ion mass spectrometry (SIMS) suggests that the State Line
98 xenoliths could represent deep crustal cumulates, rather than restites or crystallized
99 basaltic melts. We go a step further and propose that the melt that crystallized the
100 protoliths of the State Line xenoliths was hydrous (≥ 1 wt.% H₂O), based on calculated
101 H₂O contents of liquids last in equilibrium with the xenoliths. A plausible scenario for
102 such a melt could have been subduction magmatism associated with the Yavapai arc
103 terrane, one of several Proterozoic arc building blocks of the North American continent.

104 **2 Geologic setting & previous work**

105 **2.1 Geologic background**

106 The State Line Kimberlite District comprises ~100 kimberlite diatremes of
 107 Devonian age, a large number of which bear mantle and lower crustal xenoliths (Eggler
 108 et al., 1987). The diatremes were emplaced within Proterozoic continental crust of the

109 Colorado Province (Bickford
 110 et al., 1986), just south of the
 111 boundary with Archean crust
 112 of the Wyoming Craton (**Fig.**

113 **1**). The Wyoming Craton
 114 and Medicine Hat Block
 115 represent part of a number of
 116 Archean cratonic cores
 117 amalgamated in the

118 Paleoproterozoic to form the
 119 nucleus of Laurentia
 120 (Whitmeyer & Karlstrom,
 121 2007). Starting at ~1.8 Ga, a
 122 series of oceanic terranes and
 123 island arcs accreted to the
 124 southern edge of the
 125 Wyoming Craton. These

126 accreted arc terranes form
 127 large scale, northeast-
 128 trending belts with juvenile
 129 crust ages decreasing away
 130 from the cratonic core: the

131 Yavapai Province (1.7 – 1.8 Ga), the Mazatzal Province (1.7 – 1.6 Ga), and the Granite-
 132 Rhyolite Province (1.55 – 1.35 Ga). The core of the North American continent
 133 coalesced completely by ~1.0 Ga (the Grenville Orogeny).

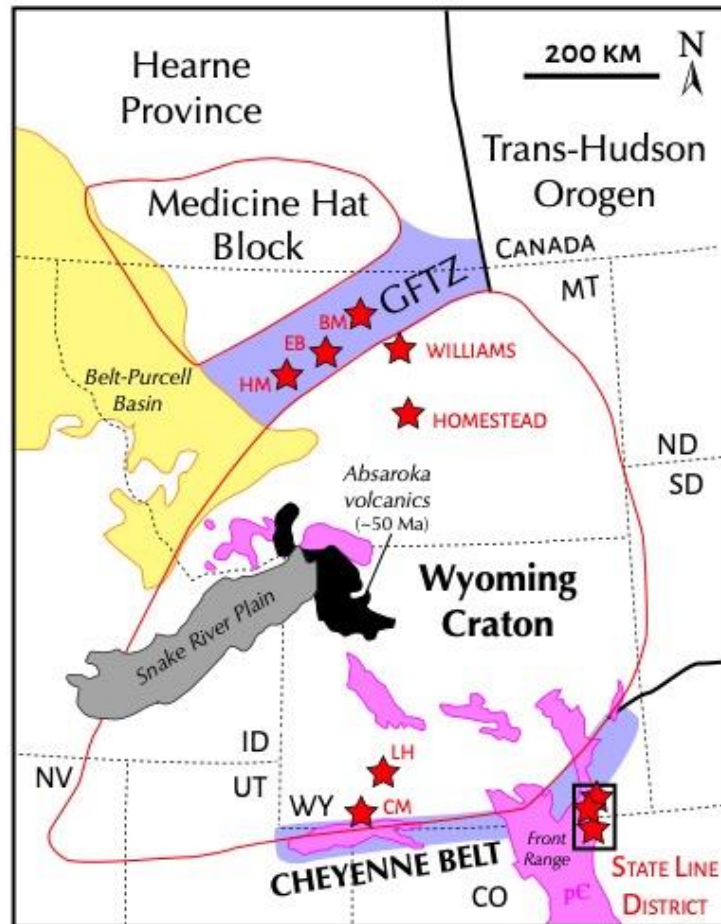


Fig. 1. Geologic & tectonic setting. Simplified map of the Wyoming Province showing key geologic features. Xenolith localities are denoted by red stars: BM = Bearpaw Mountains, EB = Eagle Butte, HM = Highwood Mountains, CM = Cedar Mountain, LH = Leucite Hills. GFTZ = Great Falls Tectonic Zone.

134 The Colorado Province remained quiescent until the end of the Paleozoic, when
135 regional deformation developed the Ancestral Rocky Mountains. The next major tectonic
136 event to impact the Colorado Province did not occur until ~70 Ma with the Laramide
137 Orogeny, classically attributed to low angle subduction of the Farallon Plate beneath
138 Western North America (Dickinson & Snyder, 1978). Low angle subduction induced
139 significant fluid metasomatism and hydration of the deep lithosphere across much of the
140 Western US (Humphreys et al., 2003). The impact of deep lithospheric hydrous
141 metasomatism is manifested by amphibole and biotite-rich lower crustal xenoliths
142 erupted in 3.0 to 0.89 Ma lamproites (Lange et al., 2000) to the northwest of the
143 Devonian-age State Line kimberlites (Leucite Hills; **Fig. 1**), as well as distinctive
144 geochemical signatures in Cenozoic volcanic rocks throughout the southwestern US
145 ascribed to melting of hydrous metasomatized continental lithosphere (Farmer et al.,
146 2020). Importantly, the xenoliths from the State Line kimberlites do not show evidence
147 for hydrous metasomatism (Farmer et al., 2005), and their Devonian eruption ages means
148 they were never impacted by the hydrous overprint of the Laramide Orogeny. Thus, the
149 State Line lower crustal xenoliths represent a potentially pristine glimpse of the water
150 content of lower continental crust preserved since its formation.

151 ***2.2 Lower crustal xenoliths***

152 Lower crustal xenoliths from the State Line District include a variety of mafic
153 lithologies, but are dominated by (nominally anhydrous) mafic granulites, with
154 subordinate amphibolites, anorthosites, and gabbroic xenoliths (Bradley & McCallum,
155 1984; Farmer et al., 2005). Within the mafic granulites, Bradley and McCallum (1984)
156 defined three groups: two pyroxene granulites, two pyroxene garnet granulites, and
157 clinopyroxene garnet granulites. The final equilibration conditions of garnet-bearing
158 granulites range from ~1 – 1.5 GPa and ~700 – 800 °C (Farmer et al., 2005). In addition,
159 xenoliths of mantle eclogite are common (Ater et al., 1984). Although most of these
160 eclogitic xenoliths are eclogites *sensu stricto* (e.g., containing omphacitic clinopyroxene),
161 a small number of xenoliths were also classified as “eclogite” by Farmer et al. (2005)
162 (e.g., sample SH-E1), but as we discuss later in this paper, some of these previously
163 classified eclogites do not resemble MORB-eclogites *sensu stricto*. Generally speaking,
164 garnet-bearing granulites are compositionally gradational to eclogites (Ater et al., 1984;

165 Bradley & McCallum, 1984). For example, Bradley and McCallum (1984) noted that the
166 mafic garnet-clinopyroxene granulites have relatively high jadeite content in their
167 clinopyroxenes, similar to the sodic clinopyroxenes in the eclogite xenoliths, suggesting a
168 gradual transition into eclogite facies. Here, we will refer to the aforementioned three
169 groups of nominally anhydrous mafic granulites collectively as “lower crustal xenoliths”
170 and divide them into two broad groups based on mineralogy: garnet-free and garnet-
171 bearing. No “true” eclogites from Ater et al. (1984), nor amphibolites, are examined in
172 this paper.

173 The modal mineralogy of the State Line lower crustal xenoliths is dominated by
174 clinopyroxene, orthopyroxene, plagioclase, and garnet; these phases constitute >90% by
175 volume of most of the xenoliths (Bradley & McCallum, 1984). Amphibole is present in
176 some 2-pyroxene granulites (Bradley & McCallum, 1984; Farmer et al., 2005), but is
177 absent or rare in garnet-bearing xenoliths. The most common accessory minerals are
178 ilmenite, rutile, and apatite. Farmer et al. (2005) also reported minor amounts of zircon,
179 barite, and K-feldspar. The latter two minerals were interpreted as grain boundary
180 contaminants from the host kimberlite, as observed in K-rich phases along grain
181 boundaries and K-feldspar occasionally replacing plagioclase grains.

182 U-Pb ages of zircons from State Line lower crustal xenoliths show a wide range of
183 dates, with a dominant population of $^{207}\text{Pb}/^{206}\text{Pb}$ dates of 1.73 to 1.6 Ga (Farmer et al.
184 2005). This age population overlaps the Yavapai Orogeny (1.71 – 1.68; Whitmeyer and
185 Karlstrom (2007)). There are also smaller populations of zircons with Archean ages
186 (presumably inherited, and only present in amphibolites), ages ~1.4 Ga ages, as well as
187 with ages coeval with the kimberlite eruption (Farmer et al., 2005). Unsurprisingly,
188 zircons are rare in the more mafic xenoliths (e.g. the garnet-bearing, two-pyroxene
189 lithologies). The oldest ages recorded by zircons in the mafic xenoliths are ~1.72 Ga,
190 with evidence of overprinting (deduced from sector zoning (Farmer et al., 2005)). In
191 summary, Farmer et al. (2005) interpreted the U-Pb age systematics of the State Line
192 xenoliths to largely reflect lower crustal growth during the Paleoproterozoic, with
193 metamorphic zircon overgrowths occurring at 1.3 – 1.4 Ga, coeval with the widespread
194 regional metamorphic event at that time in North America.

195 **3 Methods**196 **3.1 Secondary ion mass spectrometry**

197 We analyzed H₂O by ion microprobe in nominally anhydrous minerals *in situ* in
198 petrographic thin sections. New one-inch round thin sections were made from previously
199 collected xenolith material. Prior to thin section preparation, each billet was microdrilled
200 and a grain of commercially available Suprasil glass (H₂O content 0.99 ± 0.36 ppm; E.
201 Hauri, personal communication) was embedded in a central area of the xenolith (**Fig. 2b**),
202 ensuring a completely flat and well-polished surface. The purpose of the Suprasil is to
203 monitor the instrumental H₂O background, a critical factor due to the ubiquitous presence
204 of volatile-rich epoxy in petrographic thin sections and the typically low H₂O
205 concentrations of nominally anhydrous minerals.

206 To minimize the background, prior to analysis the ion microprobe was baked for ~2
207 days to attain ultra-high vacuum of $\sim 2 \times 10^{-10}$ torr. During a session, four thin sections,
208 plus a separate block with mineral standards, were simultaneously introduced into the
209 airlock at $\sim 5 \times 10^{-9}$ torr for at least 4 days, and in some cases up to 7 days, to ensure
210 complete degassing of extraneous H₂O. Analyses were obtained using a CAMECA 7f-
211 Geo SIMS, with the following operating parameters: primary Cs⁺ beam with current of
212 4.5 – 5 nA, accelerating voltage of 10 kV, rastered over a 20 x 20 μm area with a field
213 aperture limiting the secondary ion collection area to an 8 μm spot in the center of the
214 rastered area. Each analysis comprised of 2 min of pre-sputtering then 30 cycles through
215 the mass sequence ¹²C, ¹⁶O¹H, ¹⁸O, ¹⁹F, ²⁷Al, Cl and ³⁰Si. OH (or H₂O) was determined
216 by using a mass resolving power of ~5200 to separate ¹⁶O¹H from ¹⁷O; H₂O
217 concentrations were determined using calibration curves (**Supporting Information**)
218 developed using mineral standards from (Aubaud et al., 2007; Mosenfelder et al., 2011;
219 Mosenfelder & Rossman, 2013a, 2013b). During analyses, the ion image and counts
220 were monitored at all times, and any visible “hot spots” in the ion image (presumably
221 corresponding to tiny, hydrous inclusions or cracks) were noted, and corresponding
222 cycles deleted if necessary. ¹²C was used as a monitor for contamination and/or cracks.
223 Any measurements with high levels of ¹²C, ¹⁹F, or visible perturbations in the ion image
224 were not reported.

225 Owing to the wide range of Si in minerals analyzed (garnet, pyroxene, plagioclase,
226 amphibole, apatite, phlogopite), in order to minimize matrix effects we normalized
227 masses to ^{18}O , since the O contents of most silicate minerals are very similar (in contrast
228 to Si which can vary by tens of weight %). Estimation of uncertainties followed the
229 protocol outlined in Chin et al. (2016), and ranged from 10 to 15% (2 RSE). Over the
230 course of two analytical sessions, the average H_2O background ranged between ~15 and
231 ~20 ppm; we background-corrected all analyses using an average value of 23 ppm.

232 ***3.2 Electron microprobe analysis***

233 Major element composition of pyroxenes, garnet, plagioclase, amphibole, and
234 phlogopite were analyzed by electron microprobe using a CAMECA SX100 at Brown
235 University (accelerating voltage 15 kV, beam current 20 nA, spot size 1 μm). In-house
236 mineral standards and secondary mineral standards were used for calibration. Relative
237 standard deviation was <1 % for major elements and ~5 % for minor elements.

238 ***3.3 EDS mapping***

239 Energy dispersive spectroscopy (EDS) maps were obtained for selected thin sections
240 using an FEI Apreo LoVac field emission gun scanning electron microscope (SEM) at
241 UC San Diego. Operating parameters were an accelerating voltage of 20 kV, beam
242 current of 3.2 nA, and 250 μs dwell time.

243 ***3.4 EBSD***

244 Electron backscatter diffraction (EBSD) maps of selected thin sections were obtained
245 with an Oxford Instruments Symmetry EBSD detector on an FEI Apreo LoVac field
246 emission gun (SEM) at UC San Diego. Thin sections were not carbon-coated prior to
247 analysis, and maps were run in low vacuum mode. Automated EBSD maps were
248 obtained using a step size of 5 μm , working distance between 26 – 28 mm, and
249 accelerating voltage of 20 kV. Raw EBSD data were first cleaned using Oxford HKL
250 CHANNEL5 software by removing wild spikes, followed by filling of non-indexed
251 pixels down to 5 nearest neighbor pixels. Typically, cleaning was minimal as most
252 indexing rates were 90% or higher. The cleaned EBSD data were then processed in the
253 open source MTEX software to produce various types of crystal orientation maps (IPF,
254 mis2mean, GOS) and pole figures.

Sample ID	Rock type	Petrographic notes	Mineral modes
2-pyroxene granulites			
SD2-LC75	2-px granulite [†]	Medium-grained subhedral granoblastic	[26% cpx, 16% opx, 56% plag, trace oxides] ¹
SD2-LC118	2-px granulite [†]	Medium-grained subhedral granoblastic; very similar texturally and mineralogically to SD2-LC75	
NX4-LC2	2-px granulite [†]	Medium-grained subhedral granoblastic	
2-pyroxene garnet granulites			
SD2-LC120	2-px gt granulite [†]	Medium- to coarse-grained anhedral granoblastic orthopyroxene and plagioclase, with interstitial clinopyroxene and ilmenite and rutile. Garnet occurs throughout in fine-grained clusters (resembling foam), as well as in weakly developed coronas around orthopyroxene. Rutile grains are subrounded and medium-grained.	[35% plag, 30% opx, 25% gt, 10% cpx, minor ilmenite and K-feldspar, trace rutile and zircon] ²
SD2-LC71	2-px gt granulite [†]	Medium- to coarse-grained anhedral granoblastic Plagioclase contains deformation twins Garnet and clinopyroxene show a coarse myrmekitic texture organized into loosely defined coronas	[35% cpx, 12% opx, 29% gt, 23% plag, trace oxides] ¹
NX4-LC1	2-px gt granulite [†]	Medium-grained subhedral granoblastic Weak foliation defined by alignment of elongated opx, cpx, ilmenite [†] Ilmenites are widely distributed; garnet coronas appear to have nucleated predominantly on ilmenite grains Plagioclase contains deformation twins	
Opx-free garnet granulite			
SD2-LC74	Cpx-gt granulite [†]	Medium- to coarse-grained subhedral granoblastic Garnet shows various textures, from fine-grained, foamy clusters (symplectites) to coarse grains near ilmenite and clinopyroxene	[30% cpx, 30% gt, 35% plag, 3% ilm, minor K-feldspar, trace apatite, rutile, zircon, barite] ²
Xenoliths with <5 % plagioclase			
SH-E1	Eclogite [†]	Nearly bi-mineralic, very coarse-grained Large, round rutile grains dispersed throughout	[50% cpx, 48% gt, 2% rutile] ³
SD2-L110	2-px gt granulite	Resembles bi-mineralic granulites/eclogites petrographically Medium-grained subhedral granoblastic, weakly foliated with foliation defined by pyroxene or garnet-rich bands; some bands composed almost exclusively of coarse-grained clinopyroxene Plagioclase occurs interstitially between garnet and pyroxene Garnet-cpx coronas are either very small and fine-grained or absent	[40% cpx, 15% opx, 40% gt, 1% apatite, 3% plag, 1% phlogopite, trace oxide] ³
Medium grained = 1 to 5 mm; Coarse grained = >5 mm [†] classified by Farmer et al. 2005 ¹ calculated using least squares inversion of the whole-rock composition, if available (from Farmer et al. 2005) and average mineral compositions ² from Farmer et al. 2005 ³ determined by pixel counting of whole-thin section SEM EDS maps in Adobe Photoshop			

Table 1. Xenolith descriptions, petrography, and modal mineralogy.

256 **4 Data and Results**257 **4.1 Mineralogy and petrography**

258 Although previous studies (Bradley & McCallum, 1984; Farmer et al., 2005) reported
259 three distinct mineral assemblages in the State Line lower crustal xenolith suite, here we
260 will broadly describe the xenoliths as two groups: garnet-free and garnet-bearing (**Table**
261 **1**). Garnet-free (i.e., two-pyroxene granulite) xenoliths are characterized by equigranular
262 texture and numerous grains meeting at 120° triple junctions, exemplified in SD2-LC75
263 (**Fig. 2d**). Mineral modes are dominated by plagioclase (~70%), with subequal amounts
264 of clinopyroxene and orthopyroxene (~25-30% total pyroxene), and ~3-5% ilmenite. In
265 contrast, garnet-bearing xenoliths vary widely in mineral modes and textures (**Fig. 2**).
266 Many garnet-bearing xenoliths have garnet-clinopyroxene coronas formed around
267 ilmenite and plagioclase (Farmer et al., 2005). Below, we highlight notable features of
268 three garnet-bearing xenoliths that encompass the mineralogical and textural complexity
269 of the lower crustal xenolith suite.

270 SH-E1 (**Fig. 2a**) (classified as an eclogite by Farmer et al. (2005)) is very coarse-
271 grained (>1 cm) and comprised of approximately equal amounts of clinopyroxene and
272 garnet, with ~2% rutile. Clinopyroxene grains are often bent and deformed. Rutile
273 occurs as 0.15 to 1.5 mm grains with various morphologies ranging from euhedral to
274 rounded. Garnet occurs as very large (1 – 3 cm) grains with irregular, interlobate grain
275 boundaries with clinopyroxene-occupied embayments.

276 SD2-L110 (**Fig. 2b**) contains ~40% clinopyroxene, ~40% garnet, ~15%
277 orthopyroxene, ~5% plagioclase + K-feldspar, ~1% apatite, and minor ilmenite,
278 phlogopite, and hornblende. Clinopyroxene occasionally forms coarse-grained, equant
279 bands (**Fig. 2b**). Apatite is dispersed widely throughout the xenolith but is less abundant
280 in clinopyroxene-rich bands (**Fig. 2e, f**). Garnet-clinopyroxene coronas are uncommon
281 and small in size.

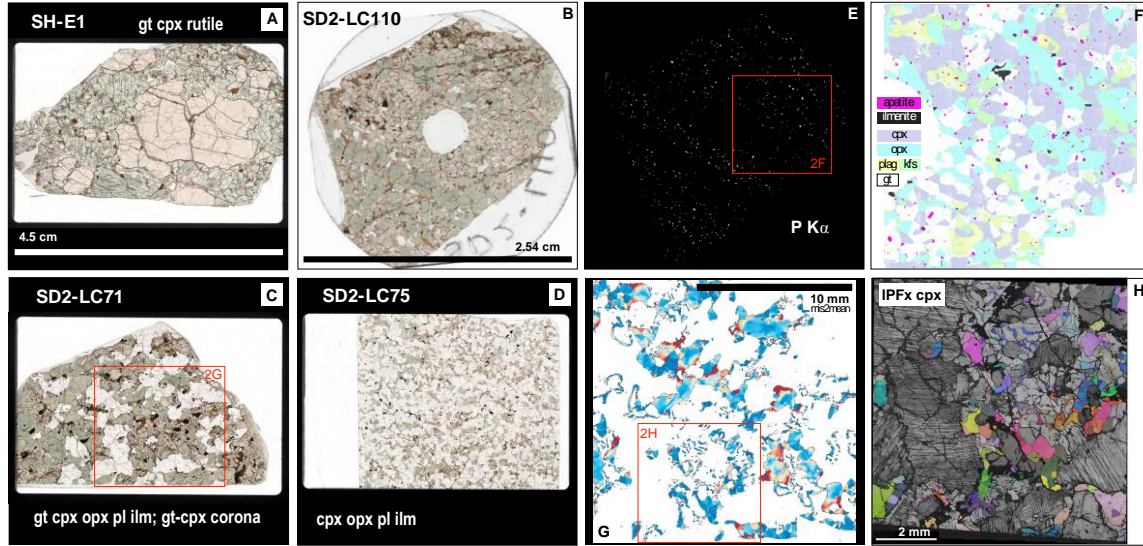


Fig. 2. Representative petrographic and microtextural features of the State Line lower crustal xenoliths. Left 4 panels (**A-D**): plane-polarized light scans of thin sections. (**B**) shows an example of a 1-inch round thin section with Suprasil glass mounted in the center for SIMS analyses (standard size thin sections are shown for other xenoliths because more area is available for observation). Right panels (**E-H**): Microbeam maps of SD2-L110 and SD2-LC71. (**E**) is an EDS map of P highlighting the widespread distribution of apatite in xenolith SD2-LC110. (**F**) shows a false-color stacked EDS map of a sub-area of E. (**G**) is a mis2mean map of clinopyroxene grains from the red outlined area in (**C**). (**H**) is the same area in (**G**) mapped by EBSD (shown here is an inverse pole figure map of clinopyroxene, superimposed on band contrast, in the x sample direction). Note abundance of deformation twins in plagioclase, as well as the similarity in IPF colors of within-corona, fine-grained clinopyroxene but more random colors in coarser-grained clinopyroxene.

282

283 SD2-LC71 contains ~25% plagioclase, ~35% clinopyroxene, ~15% opx, ~20%
 284 garnet, ~3-5% ilmenite, and trace amounts of K-feldspar. A distinctive feature of SD2-
 285 LC71 is the widespread occurrence of garnet-clinopyroxene coronas (**Fig. 2g, h**), which
 286 may comprise up to 30% or more of the xenolith. Farmer et al. (2005) noted the
 287 abundance of garnet-clinopyroxene coronas in several State Line granulite xenoliths, and
 288 interpreted the coronas to form from precursor orthopyroxene and calcic plagioclase.
 289 The coronas are irregular and lack concentric, mineral-specific zoning often seen in
 290 typical granulites (McLelland & Whitney, 1980). Within coronas, clinopyroxene occurs
 291 as small, worm-like grains surrounded by garnet (**Fig. 2g, h**); outside coronas,
 292 clinopyroxene occurs either as rims around orthopyroxene or as large porphyroclasts
 293 (**Fig. 2c**).

294 In summary, the State Line garnet-free and garnet-bearing lower crustal xenoliths
 295 constitute a relatively simple mafic mineralogy, comprising two pyroxenes, plagioclase,
 296 ilmenite, and/or garnet. Olivine is absent. Garnet-bearing xenoliths show a greater
 297 diversity of textures and deformation microstructures compared to the garnet-free group.
 298 Some of these features, such as garnet-clinopyroxene coronas, attest to textural
 299 disequilibrium (Bradley & McCallum, 1984).

300

301 **4.2 Deformation microstructures**

302 Microstructures of two xenoliths, SD2-L110 and SD2-LC71, were investigated in
 303 detail using EBSD mapping. In SD2-L110, clinopyroxene and orthopyroxene define a
 304 foliation (**Fig. 3**) and exhibit measurable, but weak, crystallographic preferred
 305 orientations (CPOs) (**Fig. 3**). The CPOs of
 306 both clinopyroxene and orthopyroxene are
 307 similar: though weak, they show [001]
 308 maxima parallel to and [010] maxima
 309 perpendicular to the apparent lineation/trace
 310 of foliation (**Fig. 3**). Such CPOs suggest slip
 311 along [001] and (010) as glide plane,
 312 consistent with naturally deformed deep
 313 lithospheric enstatites (Avé Lallemant, 1969).

314 A similar macroscopic foliation, loosely
 315 defined by garnet and clinopyroxene, is also
 316 observed in SD2-LC71 (**Fig. 2c**). Large
 317 plagioclase grains record evidence of plastic
 318 deformation, as shown by deformation twins,
 319 some of which are bent (**Fig. 2h**). Garnet-
 320 clinopyroxene textures in SD2-LC71 appear
 321 to have formed by reaction (Farmer et al.,
 322 2005), as evidenced by intricate garnet-
 323 clinopyroxene coronas forming near and
 324 around orthopyroxene, plagioclase, and occasionally ilmenite. Note that garnet and

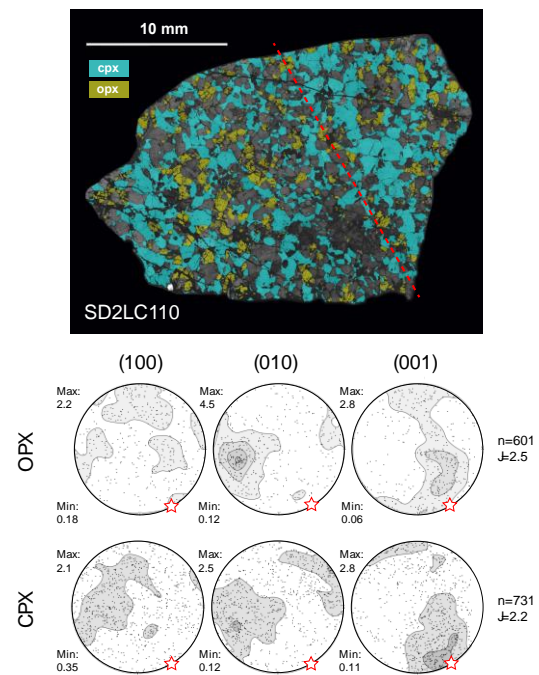


Fig. 3. Top: Large-area EBSD map of SD2-LC110. Only clinopyroxene and orthopyroxene are highlighted on top of band contrast. Dashed red line represents trace of foliation plane. Bottom: Pole figures (one point per grain) of orthopyroxene and clinopyroxene. N = number of grains, J = J index, a measure of the CPO strength.

325 clinopyroxene, together, constitute over 60% of the mineral mode (**Table 1**). Fine-
 326 grained corona clinopyroxene grains share similar crystallographic preferred orientations
 327 (based on inverse pole figure map, or IPF, in the sample reference frame; **Fig. 2h**)

328 compared to coarser grained
 329 clinopyroxene outside coronas.
 330 Interestingly, large
 331 clinopyroxene porphyroclasts
 332 appear

333 to have higher degrees of lattice
 334 distortion compared to fine-
 335 grained clinopyroxene in garnet
 336 coronas. This is shown in the
 337 mis2mean (misorientation to the
 338 mean) map in **Fig. 2g** and
 339 quantitatively in **Fig. 4**. The
 340 mis2mean measures the extent of
 341 intragranular misorientation by
 342 plotting the difference of
 343 orientation (misorientation)
 344 between the crystal's average

345 orientation and the measured orientation at a given point in the grain. Since crystal
 346 misorientations generally arise from dislocations, mis2mean maps provide a graphical
 347 representation of the extent of ductile deformation in a grain population.

348

349 **4.3 Mineral compositions: major elements and water content**

350 Clinopyroxene major element compositions from Bradley and McCallum (1984) and
 351 Farmer et al. (2005) along with new data from four xenoliths (SD2LC-110, SHE-1,
 352 SD2LC-71, SD2-LC75) are plotted against MgO in **Fig. 5**; all data are reported in **SI**
 353 **Table 1**. Clinopyroxenes are diopsidic with significant jadeitic components (Bradley &
 354 McCallum, 1984; Farmer et al., 2005) and generally unzoned with respect to major
 355 elements. The average H₂O content of clinopyroxene varies from 75 ppm to 760 ppm,

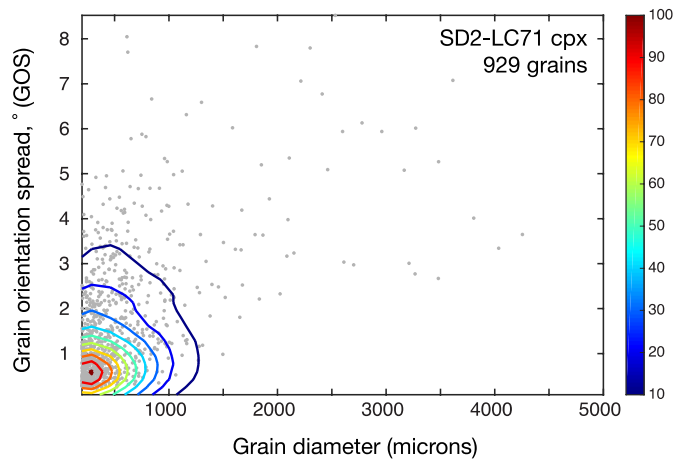


Fig. 4. Grain orientation spread (GOS) vs. grain size for 929 clinopyroxene grains in SD2-LC71. The GOS is similar to mis2mean, but reports 1 value for each grain denoting the degree of internal misorientation (higher numbers represent more intragranular misorientation). Each gray point represents 1 grain. The data have been contoured using a 2D histogram method to show that there are a large number of small grains with low GOS (these correspond to clinopyroxene inside garnet coronas) and a small number of large grains with high GOS (these correspond to clinopyroxene porphyroclasts).

356 and is inversely correlated with clinopyroxene Mg# (**Fig. 6; Table 2**). H₂O contents are
 357 relatively homogeneous within individual grains within a given xenoliths, however some
 358 xenoliths show a range of H₂O concentrations across individual grains. Generally, grains
 359 are unzoned with respect to H₂O, but a few xenoliths show grains with slightly higher
 360 H₂O in cores versus rims.

361 We report new orthopyroxene major element compositions for SD2-LC75, SD2-
 362 LC71, and SD2-L110; these data as well as selected mineral data published in Bradley
 363 and McCallum (1984) and Farmer et al. (2005) are included in **SI Table 1**.
 364 Orthopyroxene is generally enstatitic (~70%) and unzoned with respect to major
 365 elements. Average H₂O content of orthopyroxene ranges from 233 to 410 ppm (**Table**
 366 **2**).

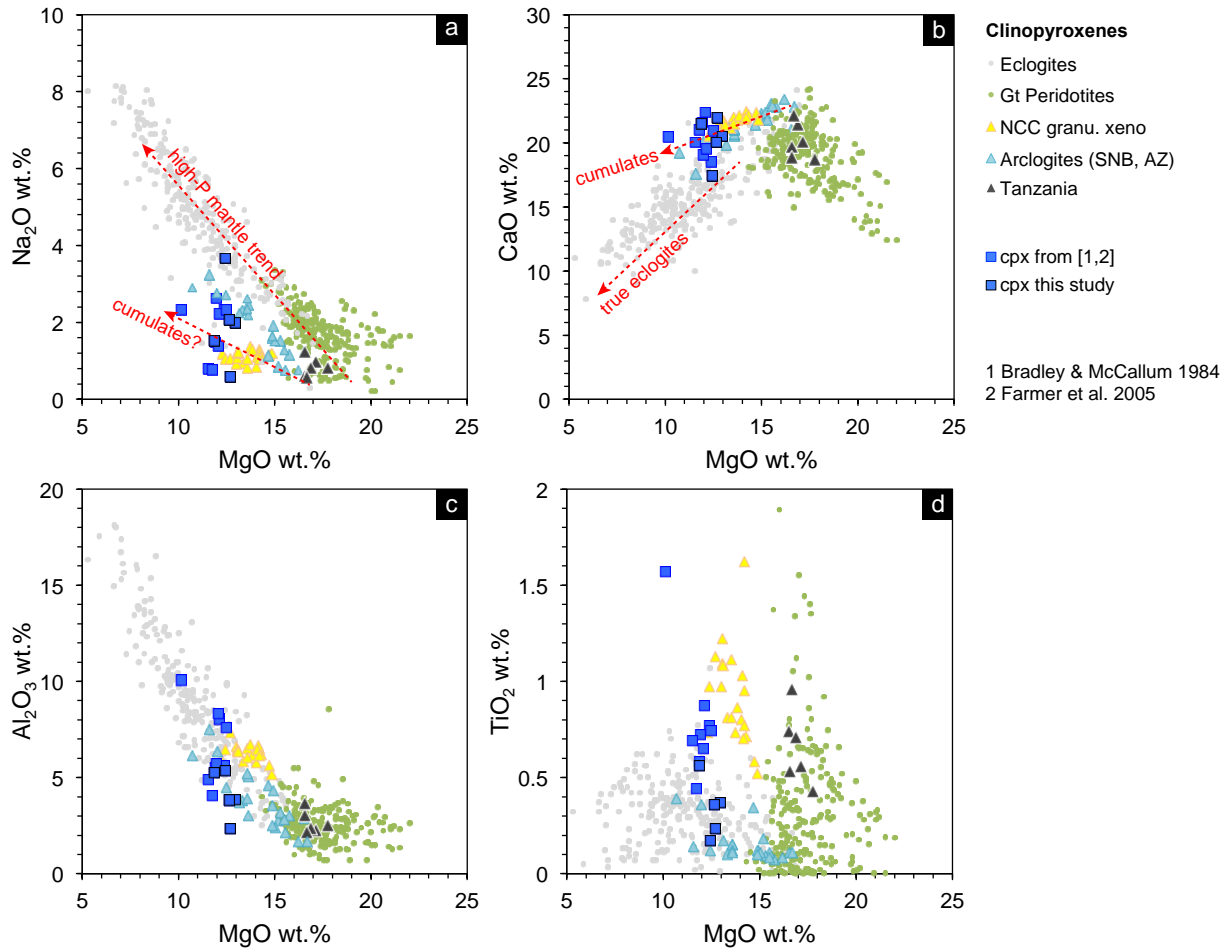


Fig. 5. Clinopyroxene compositions. Clinopyroxene major element oxides plotted against MgO (wt. %). Dashed red lines highlight general trends followed by mantle rocks (high-P mantle trend, exemplified by mantle eclogites) and distinct trend followed by cumulates. Compositions of clinopyroxenes in eclogite xenoliths are from Hills and Haggerty (1989), Fung and Haggerty (1995), Beard et al. (1996). Compositions of clinopyroxenes in garnet peridotites are from Boyd and Mertzman (1987), Ehrenberg (1982), Hervig et al. (1986), Franz et al. (1996), Reid et al. (1975). **(A)** Na₂O vs. MgO, **(B)** CaO vs. MgO, **(C)** Al₂O₃ vs. MgO, **(D)** TiO₂ vs. MgO

367

368 Major elements were analyzed in garnet from SD2-LC71, SH-E1, and SD2-L110 and
369 reported in **SI Table 2**. Garnets are pyrope-almandine. The average H₂O content of
370 garnet varies from 42 to 139 ppm and is also inversely correlated with bulk rock Mg# and
371 clinopyroxene Mg#. Garnets are unzoned with respect to H₂O and also quite
372 homogeneous in major element composition within individual grain populations in a
373 given xenolith (**SI Table 2**).

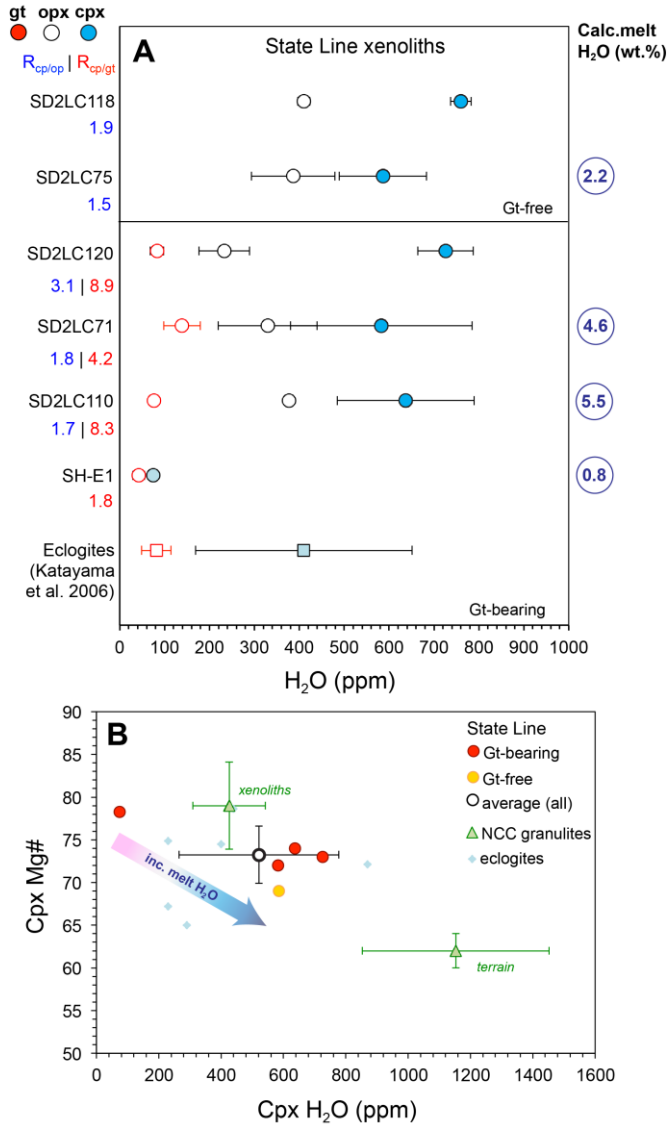


Fig. 6. Water content in major silicate nominally anhydrous minerals. H₂O (ppm) in garnet, orthopyroxene, and clinopyroxene in State Line lower crustal xenoliths. Inter-mineral ratios shown for cpx/opx and cpx/garnet on left side; calculated melt H₂O content shown on right side. See text for details. **(B)** Clinopyroxene Mg# vs. clinopyroxene H₂O (ppm). NCC granulite data from Yang et al. (2008); eclogite data from Katayama et al. (2006). Shaded arrow shows calculated trend of increasing melt H₂O with decreasing Cpx Mg#.

374

375 In addition to the modally abundant minerals clinopyroxene, orthopyroxene, and
 376 garnet, we also analyzed H₂O contents in accessory minerals apatite, phlogopite, and
 377 amphibole. These are reported in **SI Table 3**.

378 **4.4 Whole rock major element systematics**

379 Whole rock major element oxides of 15 xenoliths previously reported in Bradley and
 380 McCallum (1984) and Farmer et al. (2005) are plotted against Mg# (atomic
 381 Mg/(Mg+FeT)*100) in **Fig. 7a-d**. FeO_T and MgO are plotted against SiO₂ in **Fig. 7e** and
 382 **f**, respectively. Broadly, the State Line lower crustal xenoliths are mafic, with Mg#s
 383 ranging from 51 to 69. Average SiO₂ contents are slightly lower (48.7 wt. %) than

384 average MORB (50 wt.%). Notably, some xenoliths extend to low SiO₂ values <47 wt.%
 385 (**Fig. 7c**). The State Line xenoliths also trend towards lower CaO with decreasing Mg#
 386 compared to average MORB (**Fig. 7e**), and towards higher FeO with decreasing Mg#.
 387 We point out xenolith SH-E1, which was previously classified as MORB-type eclogite
 388 (Farmer et al., 2005) plots away from average MORB in terms of Al₂O₃ (10 wt.%
 389 compared to 15 wt.% for average MORB), MgO (13 wt.% vs 7.5 wt.%) and Na₂O (2.2
 390 wt% versus 2.6 wt.%) (**Fig. 7**).

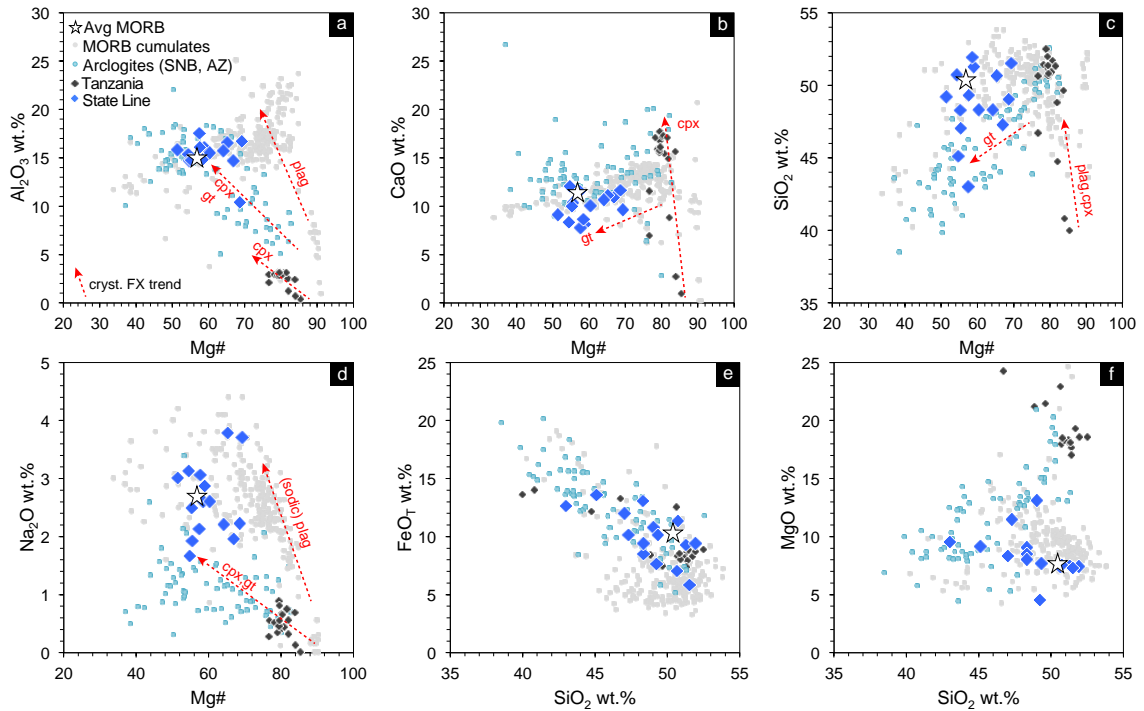


Fig. 7. Whole-rock major element systematics. Whole-rock major element oxides of State Line lower crustal xenoliths. Also plotted for comparison are average MORB, MORB cumulates, arclogites, intraplate rift cumulates (Tanzania). Dashed red lines are schematic trends corresponding to crystal fractionation of different minerals (plagioclase, clinopyroxene, etc.). **(A)** Al₂O₃ vs. Mg#, **(B)** CaO vs. Mg#, **(C)** SiO₂ vs. Mg#, **(D)** Na₂O vs. Mg#, **(E)** FeO_T vs. SiO₂, **(F)** MgO vs. SiO₂

391

392 **5 Discussion**393 **5.1 Inter-mineral partitioning of H₂O**

394 To assess equilibrium with respect to H₂O contents between minerals, we
 395 compare inter-mineral ratios of measured H₂O concentrations (“R”, **Table 2**) to
 396 experimental mineral/melt partition coefficients (“D”). Due to lack of published
 397 experimental H₂O partition coefficients for lower crustal rocks, we used experimental D
 398 values from Aubaud et al. (2004) and Tenner et al. (2009). Although these experiments
 399 pertain to mantle assemblages, our xenoliths have a broadly similar basaltic mineralogy,
 400 with the exception of olivine. We note, however, that published ranges of experimental
 401 H₂O mineral/melt partition coefficients are similar between plagioclase (0.001 – 0.006;
 402 Lin et al. (2019)) and olivine (0.0013 – 0.0021; Hauri et al. (2006)). Similar to mantle
 403 rocks, lower crustal rocks of broadly basaltic compositions contain abundant pyroxene,
 404 which has the highest DH₂O mineral/melt compared to olivine, plagioclase, and garnet.
 405 Thus, we can expect that H₂O partitioning between nominally anhydrous minerals in
 406 basaltic granulites to share some similarities with mafic and ultramafic upper mantle
 407 rocks.

		SHE1	SD2LC110	SD2LC71	SD2LC120	SD2LC75	SD2LC118
Garnet	Min	19	69	99	70		
	Max	67	102	230	104		
	Average	42	77	139	83		
	1σ	13	9.9	41	15		
	n	6	2	9	7		
Cpx	Min	62	476	345	634	486	733
	Max	96	1225	1178	835	766	775
	Average	75	637	583	726	586	760
	1σ	9.8	152	202	62	97	23
	n	11	9	11	3	5	2
Opx	Min		372	249	132	307	399
	Max		380	647	322	547	425
	Average		377	330	233	387	410
	1σ		4.4	110	56	93	14
	n		2	6	3	4	3
	R cpx/opx (avg)		1.7	1.8	3.1	1.5	1.9
	R cpx/gt (avg)	1.8	8.3	4.2	8.7		
	Bulk H ₂ O ^a	58	406	291		242	
	Bulk H ₂ O ^b	82	651	564			
	(ppm)						
	Calc melt H ₂ O ^a	0.8	5.5	4.6		2.2	
	(wt.%)						
n = number of individual grains analyzed							
1σ = 1 standard deviation calculated from total number of individual spots per mineral (at least 3 spots per grain)							
^a reconstructed using average mineral H ₂ O contents							
^b reconstructed using maximum mineral H ₂ O contents							

408 **Table 2.** H₂O content (ppm) in NAMs, inter-mineral partitioning, and reconstructed bulk
 409 H₂O and calculated melt H₂O contents. n = number of individual grains analyzed; 1σ = 1

410 standard deviation calculated from total number of individual spots per mineral (at least 3
411 spots per grain).^areconstructed using average mineral H₂O contents; ^breconstructed
412 using maximum mineral H₂O contents.

413
414 Using average mineral water contents, R_{cpx/opy} for garnet-free xenoliths SD2-
415 LC118 and SD2-LC75 are 1.9 and 1.5, respectively (**Fig. 6, Table 2**). These values agree
416 well with D values of 1.4 ± 0.3 for a garnet-free basaltic assemblage at 1 – 2 GPa from
417 Aubaud et al. (2004). R_{cpx/opy} (using average values) for garnet-bearing xenoliths SD2-
418 LC120, SD2-LC71, and SD2-LC110 R_{cpx/opy} are 3.1, 1.8, and 1.7 (**Table 2**), which also
419 overlap with the range of D_{cpx/opy} of 1.2 to 2 reported by Tenner et al. (2009) for
420 garnet-bearing systems. Using average mineral water contents, R_{cpx/gt} range from 1.8 to
421 8.3 (**Table 2**). If the maximum values for cpx and garnet water content is used, R_{cpx/gt}
422 range from 1.4 to 12. For comparison, experimental D_{cpx/gt} range from 5.5 to 14 as
423 reported in Tenner et al. (2009).

424 While the R values between minerals in our xenoliths show decent overlap with
425 experimental D's, the question arises as to whether the kimberlite eruption itself could
426 have modified mineral H₂O concentrations. Addition of H₂O from the kimberlite magma
427 into minerals was likely negligible, given that most individual mineral grains are
428 homogeneous and unzoned with respect to H₂O. Furthermore, no correlation exists
429 between mineral H₂O and grain size – if the host magma modified mineral H₂O, one
430 might expect some correlation given that large grains should retain more H₂O and smaller
431 grains either less H₂O (degassing) or gained H₂O (ingassing). A few clinopyroxene
432 grains do show slightly lower H₂O at rims compared to cores, which could indicate either
433 a limited extent of H₂O loss during eruption, or H₂O decrease due to subsolidus cooling
434 (Chin et al., 2016). In summary, there is no evidence that H₂O was added to mineral
435 grains during kimberlite eruption. While H₂O could have been lost from mineral grains
436 during eruption, the observation that inter-mineral H₂O contents largely reflect
437 equilibrium D values suggests that eruption-induced loss was also probably minimal
438 (since kimberlites erupt on extremely rapid timescales). However, H₂O “loss” – or,
439 alternatively, as we discuss later – decreased H₂O solubility within an approximate
440 equilibrium state of subsolidus cooling, indicates that our measured H₂O contents are
441 minimum bounds.

442 **5.2 Reconstructed bulk rock H₂O and calculated melt H₂O**

443 In the previous section, we established that inter-mineral H₂O ratios in the State Line
444 xenoliths fall within range of experimental mineral/melt D values. This observation
445 justifies our approach, described below, of calculating equilibrium melt H₂O contents that
446 could have last been in equilibrium with our xenoliths.

447 Before further discussing recalculated bulk rock H₂O and hypothetical melt
448 compositions, it is important to revisit the cooling history of the State Line lower crustal
449 xenoliths and the impact on measured H₂O contents. Petrographic and textural
450 observations of the xenoliths point to subsolidus cooling, such as the abundance of
451 garnet-clinopyroxene coronas interpreted to have formed at the expense of orthopyroxene
452 and plagioclase (Farmer et al., 2005). Although coronas could result from increasing
453 temperature and pressure (e.g. prograde metamorphism from medium to high-grade
454 granulites), they have also been proposed to form via isobaric cooling (due to the slope of
455 the spinel-garnet transition, **Fig. 8**); Kushiro and Yoder (1966) or cooling with
456 increasing pressure (Chin et al., 2012; Saltzer et al., 2001). We consider that State Line
457 xenoliths experienced subsolidus cooling following lower crustal stabilization sometime
458 in the Proterozoic (as previously proposed by Farmer et al. (2005)). If this is the case,
459 H₂O contents measured in nominally anhydrous minerals likely represent minimum
460 bounds, due to the lowering of H₂O solubility with decreasing temperature (cf. Zhao et al.
461 (2004)). Note that the effect of temperature on H₂O solubility is well-constrained for
462 olivine, but not for pyroxenes. Unlike olivine, some mechanisms of water incorporation
463 in pyroxene are thought to be coupled to slow-diffusing cations, such as the exchange
464 $\text{Al}^{3+} + \text{H}^+ = \text{Si}^{4+}$; Keppler and Bolfan-Casanova (2006). Thus, it might be expected that
465 the cooling effect on H₂O solubility may not be as extreme as that in olivine. Future
466 experimental work may shed new insights into H₂O solubility in minerals other than
467 olivine. What matters for the present study is that calculated melt H₂O contents using our
468 measured H₂O contents and D values are likely to be minimum bounds due to cooling.

469 If we consider that subsolidus cooling could have decreased the absolute
470 concentrations of H₂O in NAMs, but that cooling occurred such that inter-mineral H₂O
471 ratios continued to reflect ambient equilibrium conditions (as observed in inter-mineral
472 H₂O ratios), we can reconstruct bulk rock H₂O using maximum observed mineral H₂O

473 contents as a way to “see past” the effect of cooling (cf. Chin et al. (2016)). Although the
474 spread of H₂O contents within individual mineral grains is low (i.e., negligible core-rim
475 zoning), within individual xenoliths the H₂O contents of the grain population can be
476 variable (**Table 2**), but does not vary more than ~30% (RSD) within a given xenolith.
477 For instance, clinopyroxene H₂O varies from a minimum of 476 ppm to a maximum of
478 1225 ppm in SD2-LC110; out of a population of 9 clinopyroxene grains, only two grains
479 had H₂O above the average value of 637 ppm for the whole population. Within those two
480 grains with high H₂O, multiple spots yielded reproducible results (within 15%). We also
481 note that because of the time-resolved and *in situ* context of the SIMS measurements, any
482 measurements that could have been contaminated by fluid inclusions or other impurities
483 are easily resolved and can be removed during data reduction. Thus, we are confident
484 that any grains with H₂O above the average value for a given xenolith are likely to be
485 real, and still reflect minimum bounds on the naturally preserved H₂O contents. Using
486 maximum observed H₂O contents and mineral modes, reconstructed bulk rock H₂O range
487 from 82 ppm (SH-E1) to 651 ppm (SD2-LC110). In comparison, reconstructed bulk rock
488 H₂O using average mineral H₂O values give a range from 58 to 406 ppm.

489 Next, we calculate H₂O contents of melts last in equilibrium with the bulk
490 reconstructed xenolith H₂O contents (**Table 2**). To do so, we first determine a bulk DH₂O
491 value for each xenolith using experimental D values and mineral modes, which is then
492 used to calculate C_{H₂O melt}. For garnet-bearing xenoliths, we determined melt water
493 contents ranging from 0.8 wt.% (SH-E1) to 5.5 wt.% (SD2-LC110) (using average
494 mineral H₂O; if maximum mineral H₂O are used, calculated melt H₂O will be higher).
495 We calculated melt water content of 2.2 wt% for one garnet-free xenolith (SD2-LC75).
496 Calculated melt H₂O contents increase with decreasing clinopyroxene Mg# and
497 decreasing modal garnet and clinopyroxene. The calculated melt H₂O is noted next to
498 each xenolith in **Fig. 6a**.

499 **5.3 A cumulate, arclogite origin for the State Line lower crustal suite**

500 Previous studies on the State Line lower crustal granulite xenoliths lack clarity on the
501 origin and tectonic setting of the protoliths. While all agreed the protolith had to be
502 related to some form of basaltic magmatism, three competing hypotheses as to the
503 magmatic process responsible were proposed by Lester and Farmer (1998) and Farmer et

504 al. (2005): cumulates, restites, or *in situ* crystallized basaltic melt. Furthermore, the
505 tectonic setting of the protoliths (e.g., subduction zone, oceanic ridge, or intraplate rift) is
506 unclear, owing to ambiguity in interpreting bulk rock trace element data, particularly
507 highly incompatible elements (Sr, Rb, K), that may have been compromised by
508 kimberlite contamination.

509 Using our new data on H₂O concentrations in NAMs in the State Line xenoliths, we
510 provide new insights into the nature of the protoliths and their tectonic setting. A key
511 finding from our analysis of the H₂O data is that the *minimum* water content of the melt
512 last in equilibrium with the most primitive xenolith is already quite hydrous (~1 wt.%
513 H₂O) compared to typical primitive MORB (~0.1 wt%; Sobolev and Chaussidon (1996)).
514 Calculated melt water contents increase with decreasing Mg# (**Fig. 6b**), consistent with a
515 fractional crystallization trend wherein the xenoliths could represent (now
516 metamorphosed) crystal cumulates. While a similar trend might also be predicted for a
517 restite (partial melting) trend, we might expect mineral and bulk rock H₂O contents to be
518 even lower than observed if significant partial melting occurred, which should effectively
519 remove all or most of the water. It is also unlikely that the State Line xenoliths represent
520 “frozen in” basaltic melts trapped at depth, if we assume that their protoliths were
521 MORB-like in terms of H₂O content, as has been proposed for arc basement in the
522 Colorado Province (Cavosie & Selverstone, 2003). Moreover, if MORB-like melts
523 crystallized at initially shallow pressures and then cooled during thickening of a boundary
524 layer, we should expect bulk rock H₂O contents less than or equal to typical water
525 contents of primitive MORB melts, which are at least 10x lower than our bulk rock H₂O.
526 Thus, we propose that the State Line lower crustal xenoliths represent cumulates from a
527 hydrous melt.

528 Comparison of the State Line lower crustal xenoliths with other deep crustal
529 cumulates also supports an origin by crystal fractionation from hydrous magmas.
530 Although the overall major element composition of most of the xenoliths would place
531 them within the field of typical MORB olivine tholeiite (Bradley & McCallum, 1984;
532 Lester & Farmer, 1998), from **Fig. 7** it is apparent that over 50% of the xenoliths have
533 whole-rock Mg#'s greater than average MORB. In addition, the CaO and SiO₂ content of
534 most State Line lower crustal xenoliths are lower than average MORB (**Fig. 7b, c**). FeO_T

535 contents of the xenoliths also extend to higher values than average MORB (**Fig. 7e**). The
536 State Line lower crustal xenoliths also generally do not fall within the field of global
537 MORB cumulates. Although the mean Mg# of MORB cumulates (71; Chin et al. (2018))
538 is higher than the mean Mg# of the State Line xenoliths (60), the major element trends of
539 the State Line xenoliths differ from MORB cumulates. For instance, the State Line
540 xenoliths do not show Al₂O₃ enrichment at high Mg# signifying cotectic olivine +
541 plagioclase crystallization characteristic of MORB cumulates. This is manifested
542 modally by the absence of olivine in the State Line xenoliths. The State Line xenoliths
543 also plot in regions distinct from MORB cumulates in SiO₂ vs. Mg# and Na₂O vs. Mg#
544 plots (**Fig. 7c, d**).

545 The State Line xenoliths do overlap compositionally with the Sierran and Arizona
546 arclogite xenolith field. Arclogites are distinct from eclogites, the former representing
547 garnet and pyroxene-rich cumulates from primitive, hydrous arc magmas (Lee &
548 Anderson, 2015), whereas the latter are metamorphosed equivalents of basalt. The mean
549 Mg# of 60 for State Line xenoliths is similar to the range reported for low-MgO garnet
550 pyroxenites from the Sierra Nevada (Lee et al., 2006) and also the mean of ~62 for island
551 and continental arcs (Chin et al., 2018). Furthermore, the State Line xenoliths have
552 similar Al₂O₃ at a given Mg# range as low-MgO arclogites (**Fig. 7a**); their FeOT contents
553 also extend to elevated values similar to arclogites (**Fig. 7e**) and in contrast to Fe-poor
554 MORB cumulates. CaO contents are overall similar, but slightly lower, than arclogite
555 xenoliths (**Fig. 7b**). Although the SiO₂ content shows a wide range from 43 to 52 wt.%,
556 approximately half of the State Line xenoliths have SiO₂ overlapping with Sierran and
557 Arizona arclogites.

558 We compare clinopyroxene compositions from the State Line xenoliths to other
559 published data on deep lithospheric clinopyroxenes. These include clinopyroxenes from
560 global peridotite and eclogite xenoliths (see **Figure 5 caption** for references), arclogites
561 from Mesozoic arcs in Western North America (Erdman et al., 2016; Lee et al., 2006),
562 intraplate clinopyroxenite cumulates from Tanzania (Chin, 2018), and granulite xenoliths
563 from the lower crust of the North China Craton (Yang et al., 2008). The State Line
564 clinopyroxenes clearly fall off the high-pressure mantle array represented by garnet
565 peridotite and eclogite (*sensu stricto*) xenoliths; the former are confined to a narrow

566 range of Na₂O and CaO contents, while the latter trend towards high Na₂O and low CaO
567 (**Fig. 5a, b**). Clinopyroxene from granulite xenoliths from N. China are also distinct from
568 the State Line clinopyroxenes. This could be attributed to the lower modal abundance of
569 garnet in the N. China granulites – most of these granulites are garnet-free, and those that
570 contain garnet have it in abundances of 25% or less (Yang et al., 2008), in contrast to
571 garnet-bearing State Line xenoliths, which have >25% garnet. Again, similar to bulk
572 rock trends, State Line clinopyroxenes overlap most with clinopyroxenes from low-MgO
573 garnet pyroxenites from arclogite xenoliths. Similarities between State Line and low-
574 MgO arclogite clinopyroxenes are most clear in Na₂O vs. MgO, CaO vs. MgO, and Al₂O₃
575 vs. MgO (**Fig. 5a, b, c**). TiO₂ contents are overall higher than arclogite clinopyroxene,
576 but the steep vertical trend in the TiO₂ vs. MgO plot is similar to steep trends observed in
577 other cumulate-type rocks (e.g. N. China and Tanzania). One possibility for the
578 discrepancy in TiO₂ between State Line and arclogite clinopyroxene is that in many
579 arclogites, rutile was reported as an exsolution product from garnet and clinopyroxene
580 (Erdman et al., 2016; Lee et al., 2006).

581 ***5.4 Deep, hydrous fractional crystallization***

582 Based on the discussion above, H₂O systematics, whole rock, and clinopyroxene
583 compositional data all suggest that the State Line lower crustal xenoliths could represent
584 crystal cumulates from primitive, hydrous magmas. Crystallization experiments of
585 hydrous basaltic andesites at deep crustal conditions (~1 GPa) produced cumulates with
586 variable amounts of garnet, plagioclase, hornblende, clinopyroxene, and orthopyroxene
587 (Muntener & Ulmer, 2006), broadly similar (with the exception of hornblende) to our
588 xenoliths. The prevalence of hornblende in the experiments is probably due to the
589 relatively high melt H₂O contents in the starting material (4 – 8 wt.%). Hornblende may
590 have once been present in our xenoliths prior to final equilibration in the granulite facies,
591 and hornblende is present in small amounts in some xenoliths (Farmer et al., 2005).

592 Primitive melt inclusions from subduction zones worldwide show a well-defined
593 average H₂O content of 3.9 wt.% ± 0.4 (Plank et al., 2013). 5.5 and 4.6 wt. % H₂O in the
594 melt was calculated for garnet-bearing xenoliths SD2-LC110 and SD2-LC71,
595 respectively (**Table 2; Fig. 6**), which both have clinopyroxene Mg#s ~72 – 75 and high
596 modal proportions of garnet and clinopyroxene. These values are similar to those found

597 in primitive melt inclusions; interestingly, melt inclusions hosted in the most primitive
598 olivines ($>Fo_{86}$) seem to have higher H_2O than those in $<Fo_{85}$ olivine (Plank et al.,
599 2013), with some values as high as ~ 6 wt.% H_2O (Fig. 1 in Plank et al. (2013)).
600 Experimental petrology also indicates that basaltic systems at high pressures experience a
601 widened stability field for clinopyroxene (Kushiro & Yoder, 1969), and with more
602 andesitic compositions, garnet and clinopyroxene are expected to be the first liquidus
603 phases (Alonso-Perez et al., 2009). Thus, the overall modal mineralogy of xenoliths
604 SD2-LC110 and SD2-LC71 resemble experimental cumulates of crystal fractionation of
605 hydrous andesite. Below, we discuss the similarity in calculated equilibrium melt H_2O
606 with the ~ 4 wt.% H_2O average observed in arc melt inclusions.

607 While in a broad sense, we interpret the State Line lower crustal xenoliths to
608 represent cumulates from primitive, hydrous melts, it is unclear whether all the xenoliths
609 in the suite represent one crystal line of descent from a single parent magma, or
610 “instantaneous” cumulates from various (but petrologically similar) magmas. Due to the
611 nature of xenolith sampling, it is probably impossible to answer this question. Thus, it is
612 possible that the ~ 5 wt.% melt H_2O we calculated for garnet-bearing xenoliths SD2LC-
613 110 and SD2LC-71 (**Table 2**) could reflect a “snapshot” of part of the crystal line of
614 descent, and so melt H_2O would be expected to vary where a given cumulate is along that
615 line of descent. One way to “see through” to the H_2O content of the parental magma is to
616 consider the most primitive (highest Mg#) cumulates, as these cumulates would have
617 fractionated out early along the magmatic differentiation path. If we consider the most
618 primitive xenolith in our suite, SH-E1 (highest clinopyroxene Mg#) as one of the earliest
619 crystal cumulates to fractionate from a hydrous basaltic melt, the observed mineral modes
620 match the near bi-mineralic assemblages of early experimental cumulates (Alonso-Perez
621 et al., 2009) as well as natural cumulate arclogites (Lee et al., 2006). Using a simple
622 Rayleigh fractional crystallization model, assuming we start with 1 wt.% H_2O in the melt
623 (although we calculated 0.8 wt.% H_2O in equilibrium SH-E1, we use 1 wt.% for
624 simplicity; using 0.8 wt.% does not change the final result significantly), a fractionating
625 assemblage of clinopyroxene and garnet in ratios ranging from 50:50 to 25:75, and a D_{bulk}
626 = 0.004, and allow this melt to crystallize to $F = 0.4$, results in melt H_2O of ~ 4 wt.%,
627 similar to the global primitive melt inclusion average. Thus, fractional crystallization of

628 a melt with ~1 wt.% H₂O will not only produce garnet-clinopyroxene cumulates similar
629 to those observed in our samples, but can also evolve melts at ~50% crystallization with
630 H₂O contents that agree with primitive melt inclusions. We further note that more mafic
631 melts have lower critical melt fractions (Paterson et al., 1998), and so melt extraction will
632 occur at lower crystallinities and generally be more efficient compared to more silicic
633 melts. This would be facilitated even more with hydrous melts, owing to the high
634 incompatibility of water – early melts can have high starting H₂O, and with increasing
635 crystal fractionation, will become even more enriched in H₂O. This could be one way
636 that deep crustal fractional crystallization sets the stage for further magmatic evolution in
637 the middle crust, where amphibole can become stable at high melt H₂O contents
638 (Davidson et al., 2007).

639 *5.5 Geologic & tectonic implications*

640 Though now metamorphosed into the granulite facies, we propose that the State
641 Line lower crustal xenoliths were originally crystal cumulates from hydrous melts. The
642 presence of both garnet-free, plagioclase-bearing xenoliths and garnet and clinopyroxene-
643 rich xenoliths could represent two magmatic lineages with lower and higher melt H₂O
644 contents, respectively. One geologic scenario that could explain this dichotomy is the
645 following. The Yavapai arc terrane is thought to represent products of oceanic island arc
646 magmatism that accreted onto the North American continent during the Yavapai Orogeny
647 (1.8 – 1.7 Ga). During oceanic island arc magmatism, the lithosphere is generally under
648 extension and melting degrees can be moderate to high, producing primary melts at
649 shallower pressures and with lower melt H₂O (**1 in Fig. 8**). Such melts might fall more
650 along a tholeiitic trend and would produce cumulates comprised mostly of pyroxene and
651 plagioclase (gabbros).

661 generation depths and thus lower degrees of melting (Plank & Langmuir, 1988), and
662 hence higher initial melt H₂O (Chin et al., 2018). Such higher-H₂O and higher pressure
663 melts would crystallize liquidus garnet and clinopyroxene as early cumulates (**2 in Fig.**
664 **8**), represented now in the State Line xenoliths as the garnet-rich granulites. The scenario
665 proposed above could also explain the transitional nature of the State Line lower crustal
666 xenolith suite, which shows gradation from gabbros (tholeiitic trend) to more garnet and
667 clinopyroxene-rich assemblages (calc-alkaline trend). Following cooling into the
668 granulite facies, the Proterozoic State Line lower crust stabilized and was subsequently
669 tectonically juxtaposed over Archean lithosphere (Eggler et al., 1988), and then sampled
670 by kimberlites in the Devonian (**Fig. 8**).

671 The occurrence of abundant garnet-pyroxene coronas is also consistent with two,
672 or possibly more, distinct arc magma lineages that subsequently experienced P-T paths
673 governed by where they started along the solidus in **Fig. 8**. Analysis of the phase
674 boundaries in **Fig. 8** shows that near-solidus cumulates of a low pressure, tholeiitic melt 1
675 in **Fig. 8** would have to cool to a large extent to enter the garnet stability field due to the
676 slope of the spinel-garnet transition (path a). Note that garnet formation solely due to
677 isobaric cooling of plagioclase-rich protoliths, such as composition 1 in **Fig. 8**, is
678 kinetically inefficient (Chapman et al., 2017). This could explain the substantial
679 population of plagioclase-bearing granulites in the State Line suite. By contrast, near-
680 solidus cumulates of a deeper, presumably more calc-alkaline and hydrous, melt 2 in **Fig.**
681 **8** would already have spinel, clinopyroxene ± orthopyroxene, and garnet as liquidus
682 phases, and a smaller extent of cooling would immediately precipitate garnet and
683 clinopyroxene as early cumulate minerals, like xenolith SD2-L110 (path b).
684 Alternatively, a protolith starting at 1 in **Fig. 8** could undergo an increase in pressure
685 while cooling (path c) (Chin et al., 2016), which would pivot more quickly to the garnet
686 stability field due to the slope of the garnet-in boundary, allowing coronas to form
687 without a large amount of cooling. This could be the case for SD2-LC71 and the
688 “mixed” granulites that contain various proportions of plagioclase but abundant
689 garnet+cpx coronas.

690 Our EBSD data also suggest a history more complex than simple isobaric cooling
691 for the corona-bearing xenoliths. Microstructural observations in SD2-LC71 show

692 abundant deformation twins in plagioclase porphyroclasts, and large clinopyroxene grains
693 more deformed than fine-grained clinopyroxene inside garnet coronas (**Fig. 2g, Fig. 4**),
694 suggesting that delicate corona structures formed after an earlier ductile deformation.
695 Such a two-stage deformation history could be explained by a thickening + cooling path.
696 We conclude that isobaric cooling alone – a P-T path typically associated with plume
697 underplating – is likely not sufficient to account for the high modal garnet (>25 %) and
698 clinopyroxene (>30%) in many of the State Line xenoliths. Together with H₂O contents
699 in NAMs consistent with an igneous cumulate heritage and microstructural evidence of a
700 complex deformation history encapsulated between ~1.8 and ~400 Ma, we therefore
701 propose that the State Line granulites represent deep remnants of continental crust formed
702 in an evolving arc setting in the Proterozoic.

703 Finally, while garnet-rich arc cumulates are critical for facilitating delamination
704 or convective removal of thickened arc roots (Lee & Anderson, 2015), it should not go
705 unnoticed that plagioclase-bearing cumulates are also an important constituent of igneous
706 arc lithosphere. The origin of these gabbroic cumulates is less clear, since they could
707 have formed either in juvenile arcs that were subsequently accreted, or perhaps at oceanic
708 ridges. The buoyancy of gabbroic cumulates relative to garnet-bearing cumulates may
709 allow them to survive capture and suturing, thereby providing a buoyant “life raft” onto
710 which subsequent calc-alkaline continental arc magmatism may grow upon. In the Sierra
711 Nevada Batholith, archetype of a continental arc, Ducea and Saleeby (1996) showed that
712 gabbros, cumulate gabbros, and plagioclase granulites are nearly as abundant as garnet
713 clinopyroxenites within the well-studied Sierra Nevada deep lithospheric xenolith suite.
714 They further note that compositionally, the gabbroic cumulates and granulites overlap in
715 terms of major element bulk composition with garnet clinopyroxenites, indicating a
716 similar gradational spectrum observed in the State Line lower crust.

717 Parallels between the State Line xenoliths with Phanerozoic arclogites suggests
718 that arcs could have operated in a similar manner in the Proterozoic. Our data on the H₂O
719 content of granulite-facies rocks – typically thought to be “bone dry” – indicates that such
720 rocks can contain significant H₂O: up to ~1000 ppm in clinopyroxene and bulk H₂O
721 ranging ~400 to ~650 ppm. Such values are at least a factor of two higher than maximum
722 estimates for the upper mantle, the layer directly beneath the lower crust. Moreover, our

723 measured H₂O contents are likely to be minimum bounds due to decreased solubility
724 during cooling. This implies that lower crust formed in Proterozoic arcs could have been
725 just as hydrous, or even more hydrous than what is observed today.

726 **6 Conclusions**

727 We investigated the water contents of nominally anhydrous minerals, as well as modal
728 mineralogy and rock microstructure, in lower crustal xenoliths from the State Line
729 kimberlite district in northern Colorado, USA. Average water contents for minerals
730 range from 75 to 760 ppm, 233 to 410 ppm, and 42 to 139 ppm for clinopyroxene,
731 orthopyroxene, and garnet, respectively. Despite subsolidus cooling, inter-mineral water
732 partitioning largely reflects equilibrium D values, indicating closed system conditions.
733 Importantly, the coherence between measured inter-mineral partitioning and D values
734 allows us to constrain minimum bounds on water contents of melts last in equilibrium
735 with the xenoliths. Calculated melt water contents range from ~1 to ~5 wt.%. Together
736 with the high garnet and clinopyroxene mode in many of the xenoliths and their overall
737 resemblance to arclogite xenoliths from well-known arcs, we interpret the State Line
738 xenoliths to have originally been igneous cumulates from moderate to high pressure,
739 hydrous magmas associated with arc magmatism during Proterozoic accretion of North
740 America.

741 **Acknowledgments, Samples, and Data**

742 The authors are grateful for constructive reviews from XXX and to Editor XXX for
743 handling the manuscript. EJC thanks Joe Boesenberg for assistance on the Brown
744 University EPMA and Lonnie Hufford for EBSD assistance. EJC and STC thank Yunbin
745 Guan for help on SIMS. This work was supported by grants from the National Science
746 Foundation to EJC (NSF EAR 1719208 and NSF EAR 1855407). The authors declare no
747 financial interests that could be perceived as being a conflict of interest. Data archiving
748 for this research is currently underway and will be located at earthchem.org.

749 **References**

- 750
751 Alonso-Perez, R., Muntener, O., & Ulmer, P. (2009). Igneous garnet and amphibole fractionation in the
752 roots of island arcs: experimental constraints on andesitic liquids. *Contributions to Mineralogy
753 and Petrology*, 157(4), 541-558. doi:10.1007/s00410-008-0351-8
754 Arndt, N. T. (2013). The formation and evolution of the continental crust. *Geochemical Perspectives*, 2(3),
755 405-405.

- 756 Ater, P., Eggler, D., & McCallum, M. (1984). Petrology and geochemistry of mantle eclogite xenoliths
 757 from Colorado-Wyoming kimberlites: recycled ocean crust? *Developments in Petrology* (Vol. 11,
 758 pp. 309-318): Elsevier.
- 759 Aubaud, C., Hauri, E. H., & Hirschmann, M. M. (2004). Hydrogen partition coefficients between
 760 nominally anhydrous minerals and basaltic melts. *Geophysical Research Letters*, *31*(20).
- 761 Aubaud, C., Withers, A. C., Hirschmann, M. M., Guan, Y., Leshin, L. A., Mackwell, S. J., & Bell, D. R.
 762 (2007). Intercalibration of FTIR and SIMS for hydrogen measurements in glasses and nominally
 763 anhydrous minerals. *American Mineralogist*, *92*(5-6), 811-828.
- 764 Avé Lallemant, H. G. (1969). Structural and petrofabric analysis of an “alpine-type” peridotite: the
 765 lherzolite of the French Pyrenees. *Leidse Geologische Mededelingen*, *42*(1), 1-57.
- 766 Beard, B., Fraracci, K. N., Clayton, R. A., Mayeda, T. K., Snyder, G., Sobolev, N., & Taylor, L. (1996).
 767 Petrography and geochemistry of eclogites from the Mir kimberlite, Yakutia, Russia.
 768 *Contributions to Mineralogy and Petrology*, *125*(4), 293-310.
- 769 Bickford, M., Van, W., & Zietz, I. (1986). Proterozoic history of the midcontinent region of North
 770 America. *Geology*, *14*(6), 492-496.
- 771 Boyd, F. R., & Mertzman, S. A. (1987). Composition and structure of the Kaapvaal lithosphere, Southern
 772 Africa. In B. O. Mysen (Ed.), *Magmatic Processes: Physicochemical Principles* (Vol. 1, pp. 13-
 773 25): The Geochemical Society.
- 774 Bradley, S. D., & McCallum, M. (1984). Granulite facies and related xenoliths from Colorado-Wyoming
 775 kimberlite *Developments in Petrology* (Vol. 11, pp. 205-217): Elsevier.
- 776 Cavosie, A., & Selverstone, J. (2003). Early Proterozoic oceanic crust in the northern Colorado Front
 777 Range: Implications for crustal growth and initiation of basement faults. *Tectonics*, *22*(2).
- 778 Chapman, T., Clarke, G. L., Piazzolo, S., & Daczko, N. R. (2017). Evaluating the importance of
 779 metamorphism in the foundering of continental crust. *Scientific reports*, *7*(1), 1-12.
- 780 Chin, E. J. (2018). Deep crustal cumulates reflect patterns of continental rift volcanism beneath Tanzania.
 781 *Contributions to Mineralogy and Petrology*, *173*(10), 85.
- 782 Chin, E. J., Lee, C.-T. A., Luffi, P., & Tice, M. (2012). Deep Lithospheric Thickening and Refertilization
 783 beneath Continental Arcs: Case Study of the P, T and Compositional Evolution of Peridotite
 784 Xenoliths from the Sierra Nevada, California. *Journal of Petrology*, *53*(3), 477-511.
 785 doi:10.1093/petrology/egr069
- 786 Chin, E. J., Shimizu, K., Bybee, G. M., & Erdman, M. E. (2018). On the development of the calc-alkaline
 787 and tholeiitic magma series: A deep crustal cumulate perspective. *Earth and Planetary Science*
 788 *Letters*, *482*, 277-287. doi:https://doi.org/10.1016/j.epsl.2017.11.016
- 789 Chin, E. J., Soustelle, V., Hirth, G., Saal, A., Kruckenberg, S. C., & Eiler, J. (2016). Microstructural and
 790 geochemical constraints on the evolution of deep arc lithosphere. *Geochemistry, Geophysics,*
 791 *Geosystems*, n/a-n/a. doi:10.1002/2015GC006156
- 792 Collins, W. J., Murphy, J. B., Johnson, T. E., & Huang, H.-Q. (2020). Critical role of water in the formation
 793 of continental crust. *Nature Geoscience*, 1-8.
- 794 Davidson, J., Turner, S., Handley, H., Macpherson, C., & Dosseto, A. (2007). Amphibole “sponge” in arc
 795 crust? *Geology*, *35*(9), 787-790.
- 796 Dickinson, W. R., & Snyder, W. S. (1978). Plate tectonics of the Laramide orogeny. In V. Matthews (Ed.),
 797 *Laramide folding associated with basement block faulting in the Western United States*,
 798 *Geological Society of America Memoir 151* (pp. 355-366).
- 799 Ducea, M. N., & Saleeby, J. B. (1996). Buoyancy sources for a large, unrooted mountain range, the Sierra
 800 Nevada, California: Evidence from xenolith thermobarometry. *J. Geophys. Res.*, *101*(B4), 8229-
 801 8244. doi:10.1029/95jb03452
- 802 Eggler, D., Meen, J., Welt, F., Dudas, F. O., Furlong, K., McCallum, M., & Carlson, R. (1988).
 803 Tectonomagmatism of the Wyoming province. *Colorado School of Mines Quarterly*, *83*(2), 25-40.
- 804 Eggler, D. H., McCallum, M., & Kirkley, M. (1987). Kimberlite-transported nodules from Colorado-
 805 Wyoming. *A record of enrichment of shallow portions of an infertile lithosphere: Geological*
 806 *Society of America Special Paper*, *215*, 77-90.
- 807 Ehrenberg, S. N. (1982). Petrogenesis of garnet lherzolite and megacrystalline nodules from the Thumb,
 808 Navajo volcanic field. *Journal of Petrology*, *23*(4), 507-547.
- 809 Erdman, M. E., Lee, C.-T. A., Levander, A., & Jiang, H. (2016). Role of arc magmatism and lower crustal
 810 foundering in controlling elevation history of the Nevadaplano and Colorado Plateau: A case study

- 811 of pyroxenitic lower crust from central Arizona, USA. *Earth and Planetary Science Letters*, 439,
 812 48-57.
- 813 Farmer, G. L., Bowring, S. A., Williams, M. L., Christensen, N. I., Matzel, J. P., & Stevens, L. (2005).
 814 Contrasting lower crustal evolution across an Archean-Proterozoic suture: Physical, chemical and
 815 geochronologic studies of lower crustal xenoliths in southern Wyoming and northern Colorado.
 816 *Washington DC American Geophysical Union Geophysical Monograph Series*, 154, 139-162.
- 817 Farmer, G. L., Fritz, D. E., & Glazner, A. F. (2020). Identifying Metasomatized Continental Lithospheric
 818 Mantle Involvement in Cenozoic Magmatism From Ta/Th Values, Southwestern North America.
 819 *Geochemistry, Geophysics, Geosystems*, 21(5), e2019GC008499. doi:10.1029/2019gc008499
- 820 Franz, L., Brey, G. P., & Okrusch, M. (1996). Steady state geotherm, thermal disturbances, and tectonic
 821 development of the lower lithosphere underneath the Gibeon Kimberlite Province, Namibia.
 822 *Contributions to Mineralogy and Petrology*, 126(1-2), 181-198.
- 823 Fung, A. T., & Haggerty, S. E. (1995). Petrography and mineral compositions of eclogites from the Koidu
 824 Kimberlite Complex, Sierra Leone. *Journal of Geophysical Research: Solid Earth*, 100(B10),
 825 20451-20473.
- 826 Hauri, E. H., Gaetani, G. A., & Green, T. H. (2006). Partitioning of water during melting of the Earth's
 827 upper mantle at H₂O-undersaturated conditions. *Earth and Planetary Science Letters*, 248(3),
 828 715-734.
- 829 Hervig, R. L., Smith, J. V., & Dawson, J. B. (1986). Lherzolite xenoliths in kimberlites and basalts:
 830 petrogenetic and crystallochemical significance of some minor and trace elements in olivine,
 831 pyroxenes, garnet and spinel. *Earth and Environmental Science Transactions of the Royal Society
 832 of Edinburgh*, 77(03), 181-201. doi:doi:10.1017/S026359330001083X
- 833 Hills, D. V., & Haggerty, S. E. (1989). Petrochemistry of eclogites from the Koidu kimberlite complex,
 834 Sierra Leone. *Contributions to Mineralogy and Petrology*, 103(4), 397-422.
- 835 Hirth, G., & Kohlstedt, D. L. (1995). Experimental constraints on the dynamics of the partially molten
 836 upper mantle: 2. Deformation in the dislocation creep regime. *Journal of Geophysical Research:
 837 Solid Earth (1978, ài2012)*, 100(B8), 15441-15449.
- 838 Humphreys, E., Hessler, E., Dueker, K., Farmer, G., Erslev, E., & Atwater, T. (2003). How Laramide-Age
 839 Hydration of North American Lithosphere by the Farallon Slab Controlled Subsequent Activity in
 840 the Western United States. *International Geology Review*, 45(7), 575 - 595.
- 841 Jones, C. H., Mahan, K. H., Butcher, L. A., Levandowski, W. B., & Farmer, G. L. (2015). Continental
 842 uplift through crustal hydration. *Geology*, 43(4), 355-358.
- 843 Karlstrom, K., & Houston, R. (1984). The Cheyenne belt: Analysis of a Proterozoic suture in southern
 844 Wyoming. *Precambrian Research*, 25(4), 415-446.
- 845 Katayama, I., Nakashima, S., & Yurimoto, H. (2006). Water content in natural eclogite and implication for
 846 water transport into the deep upper mantle. *Lithos*, 86(3-4), 245-259.
- 847 Keppler, H., & Bolfan-Casanova, N. (2006). Thermodynamics of water solubility and partitioning. *Reviews
 848 in Mineralogy and Geochemistry*, 62(1), 193-230.
- 849 Kushiro, I., & Yoder, H. S. (1969). Melting of forsterite and enstatite at high pressures under hydrous
 850 conditions. *Carnegie Inst Washington Yearb*, 67, 153-161.
- 851 Kushiro, I., & Yoder Jr, H. (1966). Anorthite—forsterite and anorthite—enstatite reactions and their
 852 bearing on the basalt—eclogite transformation. *Journal of Petrology*, 7(3), 337-362.
- 853 Lange, R. A., Carmichael, I. S., & Hall, C. M. (2000). 40Ar/39Ar chronology of the Leucite Hills,
 854 Wyoming: Eruption rates, erosion rates, and an evolving temperature structure of the underlying
 855 mantle. *Earth and Planetary Science Letters*, 174(3-4), 329-340.
- 856 Lee, C.-T., & Anderson, D. (2015). Continental crust formation at arcs, the arclogite “delamination” cycle,
 857 and one origin for fertile melting anomalies in the mantle. *Science Bulletin*, 1-16.
 858 doi:10.1007/s11434-015-0828-6
- 859 Lee, C.-T. A., & Anderson, D. L. (2015). Continental crust formation at arcs, the arclogite “delamination”
 860 cycle, and one origin for fertile melting anomalies in the mantle. *Science Bulletin*, 60(13), 1141-
 861 1156.
- 862 Lee, C.-T. A., Cheng, X., & Horodyskyj, U. (2006). The development and refinement of continental arcs by
 863 primary basaltic magmatism, garnet pyroxenite accumulation, basaltic recharge and delamination:
 864 insights from the Sierra Nevada. *Contributions to Mineralogy and Petrology*, 151, 222-242.
 865 doi:10.1007/s00410-005-0056-1

- 866 Lester, A., & Farmer, G. L. (1998). Lower crustal and upper mantle xenoliths along the Cheyenne belt and
867 vicinity. *Rocky Mountain Geology*, 33(2), 293-304.
- 868 Li, Z.-X. A., Lee, C.-T. A., Peslier, A. H., Lenardic, A., & Mackwell, S. J. (2008). Water contents in
869 mantle xenoliths from the Colorado Plateau and vicinity: Implications for the mantle rheology and
870 hydration-induced thinning of continental lithosphere. *Journal of Geophysical Research: Solid
871 Earth*, 113(B9), n/a-n/a. doi:10.1029/2007jb005540
- 872 Lin, Y., Hui, H., Li, Y., Xu, Y., & Van Westrenen, W. (2019). A lunar hygrometer based on plagioclase-
873 melt partitioning of water. *Geochemical Perspectives Letters*, 10, 14-19.
- 874 Liu, J., Xia, Q.-K., Kuritani, T., Hanski, E., & Yu, H.-R. (2017). Mantle hydration and the role of water in
875 the generation of large igneous provinces. *Nature Communications*, 8(1), 1-8.
- 876 McLelland, J. M., & Whitney, P. R. (1980). A generalized garnet-forming reaction for metagneous rocks
877 in the Adirondacks. *Contributions to Mineralogy and Petrology*, 72(2), 111-122.
- 878 Mosenfelder, J. L., Le Voyer, M., Rossman, G. R., Guan, Y., Bell, D. R., Asimow, P. D., & Eiler, J. M.
879 (2011). Analysis of hydrogen in olivine by SIMS: Evaluation of standards and protocol. *American
880 Mineralogist*, 96(11-12), 1725-1741.
- 881 Mosenfelder, J. L., & Rossman, G. R. (2013a). Analysis of hydrogen and fluorine in pyroxenes: I.
882 Orthopyroxene. *American Mineralogist*, 98(5-6), 1026-1041.
- 883 Mosenfelder, J. L., & Rossman, G. R. (2013b). Analysis of hydrogen and fluorine in pyroxenes: II.
884 Clinopyroxene. *American Mineralogist*, 98(5-6), 1042-1054.
- 885 Muntener, O., & Ulmer, P. (2006). Experimentally derived high-pressure cumulates from hydrous arc
886 magmas and consequences for the seismic velocity structure of lower arc crust. *Geophysical
887 Research Letters*, 33(21), L21308. doi:10.1029/2006gl027629
- 888 Paterson, S. R., Fowler Jr, T. K., Schmidt, K. L., Yoshinobu, A. S., Yuan, E. S., & Miller, R. B. (1998).
889 Interpreting magmatic fabric patterns in plutons. *Lithos*, 44(1-2), 53-82.
- 890 Plank, T., Kelley, K. A., Zimmer, M. M., Hauri, E. H., & Wallace, P. J. (2013). Why do mafic arc magmas
891 contain ~4wt% water on average? *Earth and Planetary Science Letters*, 364, 168-179.
- 892 Plank, T., & Langmuir, C. H. (1988). An evaluation of the global variations in the major element chemistry
893 of arc basalts. *Earth and Planetary Science Letters*, 90(4), 349-370.
- 894 Rehfeldt, T., Jacob, D. E., Carlson, R. W., & Foley, S. F. (2007). Fe-rich dunite xenoliths from South
895 African kimberlites: cumulates from Karoo flood basalts. *Journal of Petrology*, 48(7), 1387-1409.
- 896 Reid, A. M., Donaldson, C., Brown, R., Ridley, W., & Dawson, J. (1975). Mineral chemistry of peridotite
897 xenoliths from the Lashaine volcano, Tanzania *Physics and Chemistry of the Earth* (pp. 525-543):
898 Elsevier.
- 899 Rudnick, R. L. (1995). Making continental crust. *Nature*, 378(6557), 571-578.
- 900 Saltzer, R. L., Chatterjee, N., & Grove, T. L. (2001). The Spatial Distribution of Garnets and Pyroxenes in
901 Mantle Peridotites: Pressure, Temperature History of Peridotites from the Kaapvaal Craton.
902 *Journal of Petrology*, 42(12), 2215-2229. doi:10.1093/petrology/42.12.2215
- 903 Sobolev, A. V., & Chaussidon, M. (1996). H₂O concentrations in primary melts from supra-subduction
904 zones and mid-ocean ridges: Implications for H₂O storage and recycling in the mantle. *Earth and
905 Planetary Science Letters*, 137(1-4), 45-55. doi:http://dx.doi.org/10.1016/0012-821X(95)00203-O
- 906 Tenner, T. J., Hirschmann, M. M., Withers, A. C., & Hervig, R. L. (2009). Hydrogen partitioning between
907 nominally anhydrous upper mantle minerals and melt between 3 and 5 GPa and applications to
908 hydrous peridotite partial melting. *Chemical Geology*, 262(1), 42-56.
- 909 Tommasi, A., & Ishikawa, A. (2014). Microstructures, composition, and seismic properties of the Ontong
910 Java Plateau mantle root. *Geochemistry, Geophysics, Geosystems*, 15(11), 4547-4569.
- 911 Whitmeyer, S. J., & Karlstrom, K. E. (2007). Tectonic model for the Proterozoic growth of North America.
912 *Geosphere*, 3(4), 220-259.
- 913 Yang, X. Z., Deloule, E., Xia, Q. K., Fan, Q. C., & Feng, M. (2008). Water contrast between Precambrian
914 and Phanerozoic continental lower crust in eastern China. *Journal of Geophysical Research: Solid
915 Earth*, 113(B8).
- 916 Zhao, Y.-H., Ginsberg, S., & Kohlstedt, D. (2004). Solubility of hydrogen in olivine: dependence on
917 temperature and iron content. *Contributions to Mineralogy and Petrology*, 147(2), 155-161.
- 918
- 919